Journal of Materials Chemistry C

PAPER

View Article Online
View Journal | View Issue

Cite this: J. Mater. Chem. C, 2017, 5, 10615

Photovoltaic enhancement by Au surface-plasmon effect for La doped $BiFeO_3$ films

F. Z. Li,[a] H. W. Zheng,*[a] M. S. Zhu,[a] X. A. Zhang,*[a] G. L. Yuan,[b] Z. S. Xie,[b] X. H. Li,[c] G. T. Yue*[a] and W. F. Zhang[a]

Received 27th July 2017,
Accepted 22nd September 2017

DOI: 10.1039/c7tc03371k

rsc.li/materials-c

Herein, the photovoltaic (PV) effect of ferroelectric $Bi_{0.85}La_{0.15}FeO_3$ (BLFO) films fabricated through a sol–gel method is investigated. The ferroelectric properties of the BLFO films improve compared to the undoped $BiFeO_3$ films. The application of Au nanoparticles (AuNPs) increases the open circuit voltage (V_{OC}) and short circuit current density (J_{SC}) from 0.2 V to 0.3 V and 5.3 μA cm^{-2} to 18.5 μA cm^{-2}, respectively, which could be attributed to Au surface-plasmon effects. The PV output for the BLFO film can be modulated after applying external poling voltages. Considering the ferroelectric polarization and plasmonic effects, a plausible theoretical model is constructed to depict the physical mechanism of PV enhancement for the BLFO film in detail. This work not only presents a new approach to improve the PV effect of ferroelectric films but also provides important insights into the PV mechanism of ferroelectric films.

Introduction

Ferroelectric films have been subjected to intensive research for decades in fundamental physics and have promising applications due to their intriguing spontaneous polarization and anomalous PV effect. Among the ferroelectrics, BFO has a large remnant polarization (P_r) and a rather small energy gap (E_g) of 2.7 eV with a direct transition feature, making it a potential candidate for future detectors or sensors, nonvolatile ferroelectric random access memories and as a promising PV material with a novel mechanism.[1–3] BFO films with obvious ferroelectric properties and polarization-tuned PV effects are generally prepared *via* the pulse laser deposition (PLD) method.[3–5] However, the expensive equipment required and their maintenance cost for the PLD technique have impeded its large-scale application. Chemical solution deposition of BFO has some advantages such as precise control of composition, high film quality and low cost. Therefore, it is worthwhile to prepare BFO based films and attempt to improve their microstructure and ferroelectric and photovoltaic properties.

Several studies have been conducted to investigate both the elementary physics and practical applications of BFO polycrystalline thin films using the site-engineering method.[6,7] This is because the instability of the phase structure and volatility of Bi element in pure BFO films result in a large leakage current and poor ferroelectric properties.[8] As far back as 2007, doped BFO films such as Mn-doped and La-doped BFO films have been reported.[9,10] Nevertheless, the 20% light absorption of these films still limits the improvement of the performances of PV devices. Thus, improving the light-harvesting is one of the most pressing problems. Noble metal nanostructures have been considered as a solution to the restricted light absorption in thin-film photovoltaic devices and the tuning of plasmon wavelength.[11] It has been widely reported that the combination of plasmonic nanostructures with semiconductors offers a feasible route to improve the performance of optoelectronic devices, where the mechanism of surface plasmon (SP) has mainly been ascribed to a strong light scattering effect and local field enhancement.[12–14] Although the PV effect of ferroelectric films has been widely reported, the PV property for ferroelectric films decorated with metal nanoparticles to form SP has been hardly investigated until recently.[15] A PV enhancement has been reported in PZT and Ag nanoparticle-embedded BFO films due to surface-plasmon assisted visible-light absorption; however, experimental evidence for the SP effect is insufficient or even lacking.[16,17]

In this study, we prepare BFO and BLFO films on F-doped SnO_2 (FTO) conductive glass substrates *via* a chemical solution deposition process. After that, AuNPs are deposited on the surface of the BLFO film *via* a dc sputtering technique. It is expected that the PV performance of the AuNPs modified BLFO film can be improved by incident photon scattering and

[a] Henan Key Laboratory of Photovoltaic Materials, School of Physics and Electronics, Henan University, Kaifeng 475004, China. E-mail: zhenghaiw@ustc.edu, xazhang@henu.edu.cn, yuegentian@126.com; Fax: +86-371-23881602; Tel: +86-371-23881602
[b] School of Materials Science and Engineering, Nanjing University of Science and Technology, Nanjing 210094, China
[c] Institute of Solid State Physics, Key Lab of Materials Physics, CAS, Hefei 230031, China

localized SP resonance (LSPR) at the metal surface. Interestingly, a clear SP resonance absorption peak is observed in the UV-vis absorption spectra of the AuNPs decorated BLFO films. In addition, the effect of ferroelectric polarization on the PV property of the AuNP modified BLFO films is explored. Finally, a possible model combining the energy band diagram with the SP effect is established in order to elucidate the experimental results.

Experimental

BFO and BLFO films were prepared *via* the sol–gel process and spin-coating technique. The precursor solution of BFO was prepared by dissolving 1.600 g bismuth nitride [$Bi(NO_3)_3{\cdot}5H_2O$] and 1.212 g iron nitrate [$Fe(NO_3)_3{\cdot}9H_2O$] in 4 mL 2-methoxyethanol to form a solution. Furthermore, 10 mol% excess amount bismuth nitride was used to compensate the Bi evaporation during the annealing process. Moreover, 2 mL acetic acid and 3 mL acetic anhydride were added to the solution as dehydrating agents. The viscosity of the resulting solution was adjusted by adding 100 μL ethanolamine. Finally, the molar concentration of bismuth or iron was adjusted to 0.3 mol L^{-1} by adding 2-methoxyethanol to make up a final volume of 10 mL. The precursors were stirred for 12 h to obtain a stable and homogeneous solution at room temperature. Lanthanum nitrate was used as the starting material for the growth of the BLFO films, and the preparation process of the precursor solution for BLFO was the same as that for BFO. The stoichiometric BFO and BLFO solutions were spin-coated on FTO substrates. BFO and BLFO films were obtained by spin coating at 800 rpm initially for 10 s and then at 4000 rpm for 30 s in ambient conditions, followed by pyrolyzing at 350 °C for 5 min. This coating process was repeated several times to obtain the desired film thickness. Finally, the films were annealed at 600 °C in air for 25 min. To examine the effect of surface plasmon on the photovoltaic properties, AuNPs were deposited onto the surface of the films for 25 s by dc sputtering (KYKY, SBC-12), followed by annealing at 450 °C in an Ar atmosphere for 3 h. For the convenience of measuring the electric behavior, circular ITO dot arrays served as the top electrode with an area of 0.0625 mm^2, which were sputtered on the surface of the films with a shadow mask. The ITO layer was deposited by radio-frequency sputtering (JGP-450A) at room temperature with a sputtering power of 80 W and working pressure of 2 Pa.

The structural properties of the films were determined by X-ray diffraction (XRD, DX-2700) with CuKα radiation. The optical absorption spectrum of the films was obtained using a UV-visible spectrophotometer in the wavelength range of 300–800 nm. (Varian Cary 5000). The thickness of the films was examined *via* field emission scanning electron microscopy (FE-SEM, JSM-7001F). The macroscopic and microscopic ferroelectric properties of the films were measured with a Precision workstation (Radiant Technologies, Inc USA) and a piezoresponse force microscope (PFM, Multimode 8), respectively. Atomic force microscopy (AFM, Multimode 8) was employed to evaluate the size of the AuNPs. Mott–Schottky analysis of the BLFO thin films was performed on an electrochemical workstation with capacitance impedance measurements in aqueous electrolyte (Wuhan Corr-Test Instrument Co. Ltd). Current density–voltage (*J–V*) curves were measured using a Keithley 2400 source meter and a low noise probe station in the dark and under the illumination of white light (solar simulator, 100 mW cm^{-2}, AM 1.5). All measurements were conducted at room temperature. The band edge of the BLFO film was obtained *via* ultraviolet photoelectron spectroscopy (UPS, ESCALAB-250XI). The photon energy of the UV source was He I discharge at $h\nu$ = 21.21 eV.

Results and discussion

The surface SEM image of the BLFO film is displayed in Fig. 1a, which shows that the film exhibits a dense and smooth surface. From the cross-section SEM image of BLFO/FTO presented in Fig. 1b, the interface between BLFO and FTO can be clearly seen, and the thickness of BLFO and FTO is 476 nm and 338 nm, respectively. Fig. 1c shows the X-ray diffraction (XRD) patterns of the as-prepared BFO and BLFO thin films, where the sharpness of the diffraction peaks indicates high quality polycrystalline films. No peaks from impurity phases are observed within the diffractometer limitation, except for those from FTO. Most of the diffraction peaks such as (100), (110), (200), and (210) can be indexed according to the standard powder diffraction data of the $BiFeO_3$ crystal with a perovskite structure. The position of the BFO diffraction peaks shifts towards low diffraction angles with La^{3+} doping, which can be attributed to the change in the lattice parameter. According to the Bragg's equation, the diffraction angle decreases and the diffraction peaks shift towards lower angles since the ionic radius of La^{3+} (1.03 Å) is larger than that of Bi^{3+} (0.96 Å). Similar variations in XRD peaks upon rare earth-doping have been previously reported.[18–20] In the BLFO thin films, merging of the (110)/(1$\bar{1}$0) peaks is observed, which suggests that the rhombohedral distortion of the undoped BFO film decreases toward an orthorhombic or

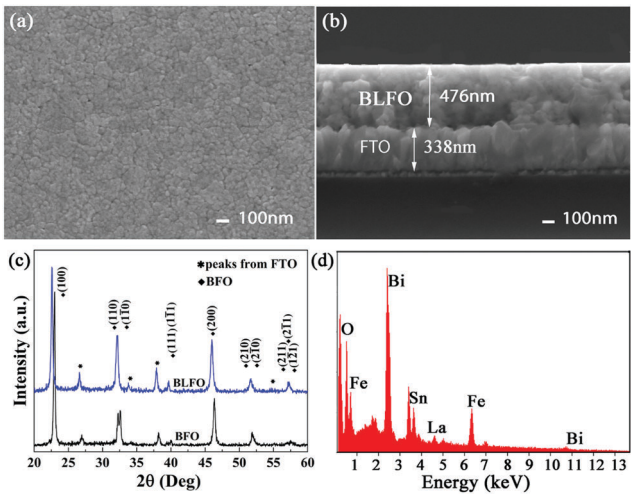

Fig. 1 (a) and (b) Surface and cross-section SEM images of BLFO film, respectively. (c) XRD patterns of the BFO and BLFO films on FTO/glass substrate. (d) EDS patterns of the BLFO film.

tetragonal structure after La doping.[21] As indicated by the XRD pattern, the incorporation of La ions into the Bi-sites induces structural distortion, which is beneficial for the improvement of ferroelectric properties.[8] Furthermore, the polycrystalline BLFO film with natural random roughness could provide the probability of coupling between the incident photons and SPs at the surface of the Au nanoparticles.[16] The substitution of lanthanum at the Bi-sites in the BFO film was further confirmed by energy dispersive spectroscopy (EDS) analysis, and the results are depicted in Fig. 1d. The EDS analysis shows that the spectrum of the film consists of Bi, Fe, La and O peaks. No other elements are detected besides the Sn element, which originates from the FTO substrate.

The P–E hysteresis loops of the BFO and BLFO films are presented in Fig. 2a with the measured frequency of 10 kHz. It is found that the BFO film displays an unsaturated P–E hysteresis loop with a low coercive field of 75 kV cm^{-1}. In contrast, the BLFO film exhibits a saturated hysteresis loop with a well saturated shape compared with the BFO film. The P_r of the BLFO film is 17 μC cm^{-2}, which is similar to that reported previously.[22,23] The improved P_r can be attributed to the structure distortion upon La doping, which was described by the XRD patterns demonstrated in Fig. 1c. We also used the PFM technique to characterize the ferroelectricity of the films. Fig. 2b and c present the typical out-of-plane (OP) PFM phase images of the BFO and BLFO films, respectively. For each image, 3 × 3 μm^2 and 1 × 1 μm^2 regions were polarized with 10 V and −10 V sample biases on the FTO bottom electrode, respectively, and then the PFM phases were instantly scanned with an ac probing voltage. As seen in Fig. 2b, the weak color contrast of the two polarized regions demonstrates poor domain switching behavior and weakened ferroelectricity for the BFO film. However, the distinct color contrast of the PFM phase image observed in Fig. 2c reveals that the ferroelectric domains switched to two opposite orientations, which indicates complete domain reversal, and electrically writable and good local ferroelectric properties for the BLFO film. Comparing Fig. 2c with 2b, it is obvious that the BLFO films possess better ferroelectricity than those of BFO, which is consistent with the macroscopic ferroelectric measurement results depicted in Fig. 2a. The representative phase/amplitude *versus* tip bias curves for the BFO and BLFO films are shown in Fig. 2d and e, respectively. Although both BFO and BLFO films show phase loops with nearly 180° switching and butterfly-like amplitude loops, it is easy to discern that the BLFO film demonstrates a broader phase hysteresis loop and higher amplitude intensity than that of the BFO film, which further supports the aforementioned experimental phenomenon that the BLFO film has superior ferroelectric properties than the BFO films. After investigating the macroscopic and microscopic ferroelectric properties of the films, we performed light absorption and PV measurements on the films.

Fig. 3a shows the UV-vis absorption spectra of the BFO and BLFO films. The spectra exhibit a broad absorption band between 400 and 550 nm, which means that the films can absorb a considerable amount of visible light, which implies their potential application as an active material for visible light absorption. More interestingly, the BLFO film exhibits a stronger absorption in the wavelength range of 400 to 500 nm compared to the BFO film, which may be related to the reduced optical bandgap after La doping. The corresponding optical band gaps can be estimated from the $(\alpha h\nu)^2 - (h\nu)$ plot by extrapolating the linear portion of $(\alpha h\nu)^2$ to zero, where α, h, and ν are the absorption coefficient, Planck constant and light frequency, respectively. As seen from Fig. 3b, the calculated value of the bandgap for the BFO film is 2.7 eV, which is close to that reported in the literature.[2,24,25] However, the bandgap value for the BLFO film is 2.63 eV, which suggests that La doping indeed reduces the optical bandgap of the BFO film. The decrease in the optical bandgap of BFO after La doping may be ascribed to two possible factors. One is related to the structural transition (reduction in rhombohedral distortion), which has been

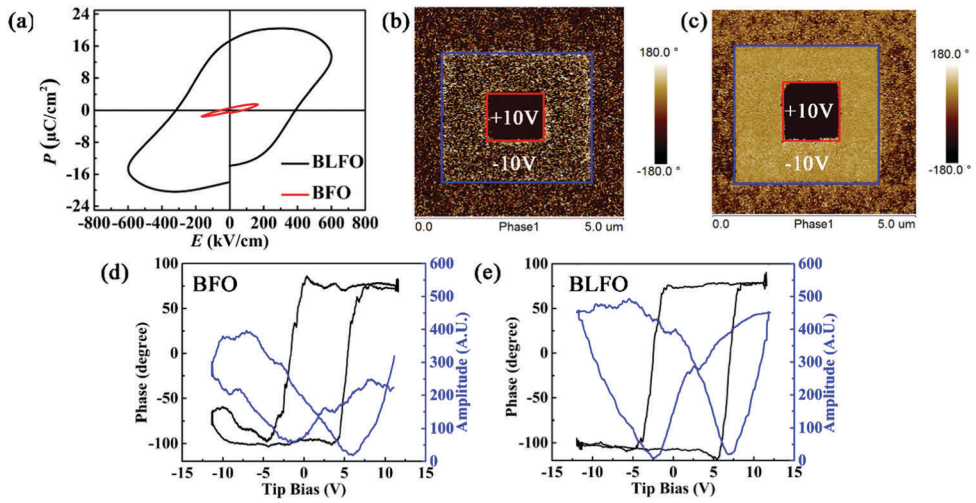

Fig. 2 (a) Hysteresis loops of the BFO and BLFO films. Out-of-plane (OP) PFM phases of the (b) BFO and (c) BLFO films. OP phase and amplitude *versus* tip bias loops of the (d) BFO and (e) BLFO films.

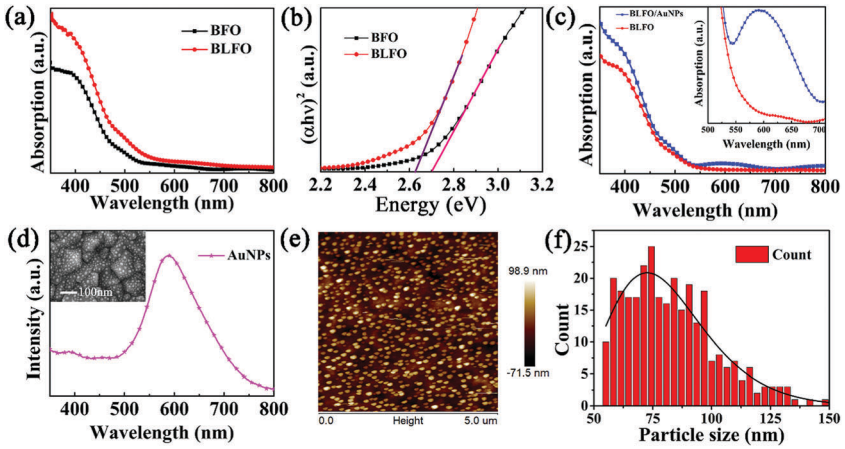

Fig. 3 (a) UV-vis absorption spectra of the BFO and BLFO films. (b) Plot of $(\alpha h\nu)^2$ as a function of $h\nu$ around the absorption edge. (c) UV-vis absorption of the BLFO and BLFO/AuNPs films and the inset is the magnification in the wavelength region of 500–700 nm. (d) Absorbance spectra of AuNPs, and the inset is the SEM image of the AuNPs. (e) AFM image of the as-prepared AuNPs on the surface of the BLFO films. (f) Size histogram of AuNPs.

reported to decrease the optical bandgap of BFO.[26] Moreover, La doping in BFO may increase the density of state in the valence band and change the position of the conduction band, resulting in a shift in the absorption edge toward a lower photon energy and thus a reduction in optical bandgap.[27,28] Fig. 3c was employed to study the light absorption characteristics of the BLFO film with and without AuNPs. It can be found that the absorption intensity of BLFO with AuNP structures is higher than that of bare BLFO, particularly in the visible region. As presented in the inset of Fig. 3c, the absorbance spectrum of BLFO loaded with AuNPs exhibits a prominent peak located at about 590 nm, and the profile of this peak is consistent with the absorption spectrum of AuNPs.[11,29,30] The reason for the emergence of the absorption peak at about 590 nm is the occurrence of the SP effect for BLFO loaded with AuNPs, which can couple and trap light into the ferroelectric film, thus enhancing optical absorption, and finally resulting in an enhanced production rate of photo-excited carriers. Moreover, as shown in the inset of Fig. 3c, the absorption peak of AuNPs is an expression of the surface plasmon resonance effect, which has been reported in literature concerning AuNP enhanced photovoltaic properties.[31–33] In addition, sputtering is one of the common approaches to deposit AuNPs, which can produce SP effects to enhance the conversion efficiency of photovoltaic devices.[34,35] Fig. 3d shows the UV-vis absorption spectrum of pure AuNPs, in which the position of the absorption peak matches well with that in the inset in Fig. 3c. This further demonstrates that the existence of the SP effect in the AuNPs–BLFO hybrid structure originates from the AuNPs. As can be observed from the SEM image (the inset of Fig. 3d), the AuNPs have a spherical morphology. For an accurate description of the size distribution of the AuNPs, the AFM image of the BLFO film decorated with AuNPs is shown in Fig. 3e. According to the statistical distribution obtained from the Nano-Scope Analysis software in Fig. 3f, the typical diameters of these spherical AuNPs are in the range of 50–150 nm with an average diameter of about 70 nm.

In order to study the effect of ferroelectric polarization on PV performance, *J–V* measurements were carried out under illumination. For comparison, *J–V* curves in the dark were also measured. As shown in Fig. 4a, although the BFO film clearly exhibits a PV effect, the polarization has almost no influence on the PV performance of the BFO film. From Fig. 4b and its inset, the J_{SC} and V_{OC} of the ITO/BLFO/FTO device under the conditions of negative bias (−10 V poled), no bias (unpoled) and positive bias (+10 V poled) are 2.8 μA cm^{-2} and 0.195 V, 5.3 μA cm^{-2} and 0.2 V, and 8.3 μA cm^{-2} and 0.22 V, respectively. Consequently, it can be found that the BLFO film has different PV response parameters with the variation in polarization states, which indicates that the PV effect of the La doped BFO film can be modulated by ferroelectric polarization. A similar experimental phenomenon for the modulation of the PV effect by polarization has also been reported in some ferroelectric films such as PZT, Bi_2FeCrO_6 and Si doped HfO_2.[36–38] In addition, the ON–OFF property under periodic exposure of light at short-circuit conditions is manifested in Fig. 4c, which further verifies the modulation of the PV effect for BLFO film. Although the ferroelectric properties of the spin-coated BLFO thin films are not comparable with films prepared by high-vacuum techniques, the P–E hysteresis loop, as a function of test voltages shown in Fig. 2a, still clearly reveals the existence of ferroelectric hysteresis in the samples. This provides an effective platform to tune the internal electric field induced by remnant polarization and thus manipulation of the photo-induced charge separation and transportation of ITO/BLFO/FTO devices.

To illustrate the mechanism of the polarization tuned PV effect, possible schematic energy band diagrams under poled conditions were constructed. The UPS spectrum of BLFO is shown in Fig. 5a. The work function (ϕ) of BLFO calculated by subtracting the spectrum width from the photon energy of the exciting radiation (21.21 eV) is ascertained to be 4.81 eV. The energy level of the valence band maximum (VBM) of BLFO, $E_F - E_{VBM}$, was obtained by extrapolating the linear portion of the low binding energy edge of the peak to the energy X axis. As presented in Fig. 5a, the value of $E_F - E_{VBM}$ for BLFO is

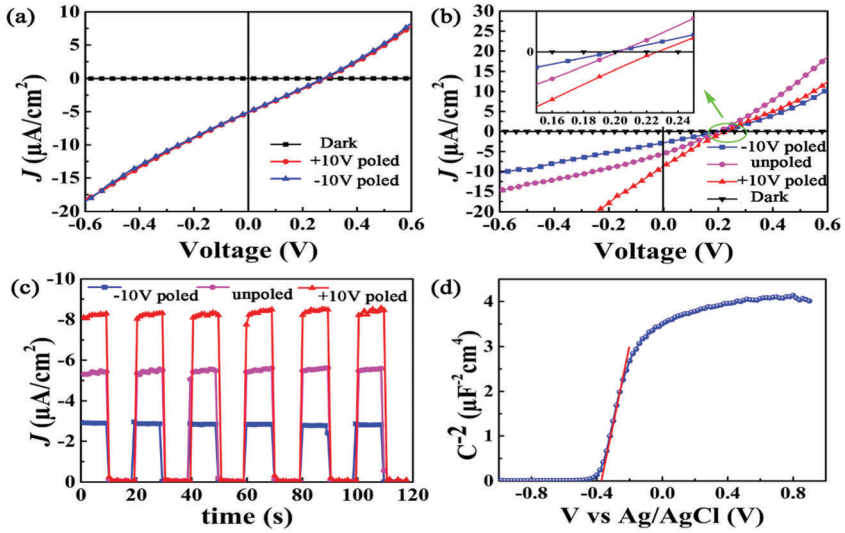

Fig. 4 J–V curves for the BFO (a) and BLFO (b) films polarized with negative and positive voltages. The inset in Fig. 5b corresponds to the enlarged region, which identifies the values for V_{OC}. (c) Time-dependence of photocurrent density under the short-circuit condition with the light being switched ON and OFF. (d) Mott–Schottky curve of the BLFO thin film.

determined to be 1.46 eV. The energy level of the conduction band maximum (CBM) of BLFO, $E_F - E_{CBM}$, could be estimated to be 1.17 eV considering that the E_g for BLFO is 2.63 eV, as shown in Fig. 3b, which indicates that the BLFO films can be regarded as n-type semiconductors. The n-type conductive behavior of the BLFO film was also confirmed by the capacitance (C) as a function of the applied photoelectrode potential (V), as exhibited in Fig. 4d, according to the positive slope in the Mott–Schottky plot.[39] Moreover, the work functions for ITO and FTO were reported to be 4.8 and 4.4 eV, respectively.[37,40] Combining the UPS data of BLFO and the work functions of ITO and FTO, the energy-level diagrams of each component materials utilized in the BLFO photovoltaic device are plotted and presented in Fig. 5b.

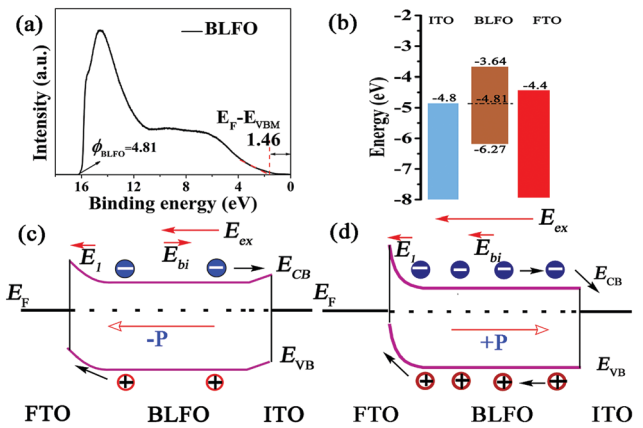

Fig. 5 (a) UPS spectra of the BLFO film. (b) Energy-level diagram based on UPS results indicating the conduction and valence energies of each component material involved in the BLFO device structure. Schematic representation of the energy band diagram of the ITO/BLFO/FTO device. Negative (c) and positive (d) poled states.

If a positive polarization voltage is applied, a Schottky barrier with the electric field pointed from BLFO to FTO will be formed due to the existence accumulated negative charges, rather than only an ohmic contact at the FTO/BLFO interface due to the similar work function of BLFO and FTO. A similar reversal of contact characteristic at the interface of the metal/semiconductor caused by ferroelectric polarization has also been reported previously.[41,42] Moreover, the positive polarization causes the interface of BLFO/ITO to be covered with positive charge and thus an ohmic contact is easily formed at this interface. When a negative polarization voltage is applied, the interface at BLFO/FTO aggregates positive charges, thus lowering the Schottky barrier height.[37,43] Likewise, the interface at BLFO/ITO gathers negative charges, thus making the ohmic contact a Schottky contact. It should be noted that the short-circuit current does not reverse whether positive or negative polarization is applied according to the aforementioned experimental results, which demonstrates that the height of the Schottky barrier of the BLFO/FTO interface is higher than that of the BLFO/ITO interface. Based on the above analysis, the energy band diagrams of the BLFO device under negative and positive poling are schematically shown in Fig. 5c and d, respectively. Herein, we define the FTO/BLFO Schottky electric field as E_1. Correspondingly, the depolarization field in BLFO is defined as E_{bi}. It is reported that the depolarization field originating from the incomplete screening of ferroelectric polarization charges is vital for the separation and transportation of photo-generated carriers.[44] Moreover, it is usually considered that a depolarization field (E_{bi}) in the direction opposite to the applied poling bias can be developed when the ferroelectric film is in a negative or positive poling state. In the negative poling state (shown in Fig. 5c), it is obvious that the Schottky barrier (E_1) at the interface of BLFO and FTO has an opposite direction to that of E_{bi}. Therefore, the total electrical field ($E_{ex} = E_1 - E_{bi}$) for driving the separation

and transportation of photo-generated carriers decreases compared with that under no poling, thus causing a weakened PV performance in the negative poling state. Furthermore, it is reasonably inferred that the magnitude of E_1 is stronger than that of E_{bi} since both the V_{OC} and J_{SC} have a consistent direction at no polarization or negative poling state. When the BLFO film is under a positive poling state, it can be found that E_{bi} has the same direction with that of E_1 (as seen in Fig. 5d). Under this circumstance, the total electric field can be enhanced and thus the driving force for the separation and transportation of photo-generated carriers improves, thus leading to a better PV effect than that at no poling or negative poling state.

The function of metal doping and AuNPs modification on tuning the photocurrent in BLFO upon illumination was explored and depicted in Fig. 6a. Herein, it is noticed that the short-circuit current density of the BLFO films (5.3 μA cm^{-2}) is higher than that of the BFO films (3.6 μA cm^{-2}). As mentioned earlier, La doping can reduce the optical bandgap of BFO (Fig. 3b), which is beneficial for absorbing more visible light, producing more photo-generated carriers and thus tailoring PV properties toward a higher performance. Although La doping reduces the bandgap of BFO films and improves their PV effect, their limited absorption of the solar spectrum still necessitates developing new absorption mechanisms.[45] Generally, Au exhibits relatively higher stability than other metals (*e.g.* Ag and Cu), and thus it is the most widely employed metal in common inorganic and organic semiconductors with an SP enhanced PV effect.[14,46] The *J*–*V* curves for BLFO with and without AuNP decoration under the illumination of white light are also given in Fig. 6a, in which the J_{SC} and V_{OC} are observed to be 18.5 μA cm^{-2} and 0.3 V and 5.3 μA cm^{-2} and 0.2 V, respectively. The experimental results clearly indicate that the AuNP decorated BLFO film has a significantly improved PV performance compared to BLFO without AuNPs. The remarkable enhancement of the PV effect can be explained as follows. On one hand, the AuNPs on top of the BLFO film drive the light preferentially into the BLFO layer itself, introducing an angular spread that increases the effective light path and thus the optical absorption. It has been reported that the size of noble metal nanoparticles has a significant influence on the mechanism of plasmonic resonance. For noble metal nanoparticles, larger than 50 nm in diameter, the far-field scattering is more likely to occur.[47] Thus, far-field scattering probably plays a dominant role in the present case considering the size distribution of the AuNPs shown in Fig. 3f. On the other hand, an ohmic contact is easily formed at the interface of BLFO/ITO because of negligible contact resistance, due to which the hot-electron transfer cannot operate well.[48] Furthermore, the negative short-circuit current and positive open circuit voltage obtained from the *J*–*V* curves under illumination imply the movement of electrons from FTO to ITO in the interior of the photovoltaic devices. If hot electron injection and transfer occur, the direction of electron movement will be from ITO through BLFO to FTO, which contradicts the observed experimental results. Specifically, the mechanism of hot-electron transfer does not match the present case. Besides, near-field enhancement by LSPR may also play an important role in the device, which can intensify the optical field near the metal surfaces and thus improve the absorption of incident photons in the BLFO film. For the PV devices, the near field enhancement can contribute to the enhancement of photocurrents and power conversion efficiencies.[49] Although SP has been reported in $BaTiO_3$ based ferroelectric materials with Au or Ag,[50,51] the SP effect has not been used to reinforce the PV property of ferroelectric materials based on strong experimental evidence so far. Moreover, Chu *et al.* investigated the photoelectrochemical properties of Au/BFO heterostructure photoelectrodes, in which hot electrons derived from SP resonance excitation participate in the water splitting process.[15] To the best of our knowledge, this study provides a simple and robust approach to effectively improve the PV performance of ferroelectric films by directly using SP effect for the first time. Furthermore, as demonstrated in Fig. 6b, the PV performance of the BLFO film decorated with AuNPs can also be modulated by ferroelectric polarization. It is obvious that the V_{OC} and J_{SC} for the −10 V poled, unpoled and +10 V poled ITO/AuNPs/BLFO/FTO devices are 0.37 V and 11.4 μA cm^{-2}, 0.3 V and 18.5 μA cm^{-2} and 0.4 V and 20 μA cm^{-2}, respectively. Therefore, positive poling can improve the PV effect, whereas negative poling weakens the PV output. The PV performance tuned by ferroelectric polarization for the BLFO film decorated with AuNPs exhibits the same variation trend as that of the BLFO film without AuNPs, which indicates a similar physical mechanism of PV effect by ferroelectric polarization. Comparing the BLFO film modulated by positive poling and under the synergistic effect of AuNP SP and positive poling, the V_{OC} and J_{SC} of the BLFO film can be tuned from 0.22 V to 0.4 V and from 8.3 μA cm^{-2} to 20 μA cm^{-2}, respectively, corresponding to the tunabilities of 90% and 140%, respectively. In order to further analyze the correlation between positive poling and AuNP SP, we compared the V_{OC} and J_{SC} for the BLFO samples under different experimental conditions, as indicated in Table 1. Herein, for simplicity, a set of BLFO films were measured unpoled and with no AuNPs, only positive poled, only AuNPs and a combination of positive polarization and AuNPs, which were labeled as I, A, B and AB, respectively. Table 2 depicts the tunability based on the data from Table 1. The data in Table 2 suggests that the AuNP SP effect plays a dominant role in improving the PV performance although

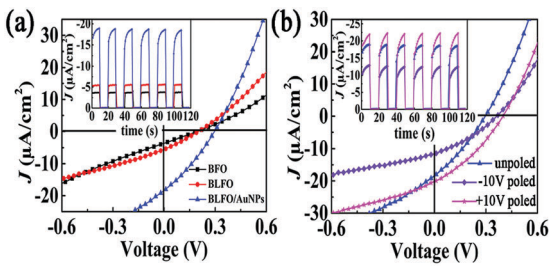

Fig. 6 (a) *J*–*V* curves for BFO, BLFO and BLFO/AuNPs under white light illumination. The inset shows the corresponding time-dependent J_{SC} with the light ON and OFF. (b) *J*–*V* characteristics of the BLFO film decorated with AuNPs at negative, positive and no poling states. The inset indicates the photocurrent as a function of time under white light illumination at an interval of 10 s.

Table 1 The J_{SC} and V_{OC} of I, A, B and AB. Here, the BLFO films measured with unpoled and no AuNPs, only positive poled, only AuNPs and combination of positive polarization and AuNPs are denoted as I, A, B and AB, respectively

Sample tested at different conditions	J_{SC} (μA cm^{-2})	V_{OC} (V)
I	5.3	0.2
A	8.3	0.22
B	18.5	0.3
AB	20	0.4

Table 2 The tunability of J_{SC} and V_{OC} for A, B and AB to I

Tunability	J_{SC} (%)	V_{OC} (%)
A to I	56.6	10
B to I	249	50
AB to I	277	100

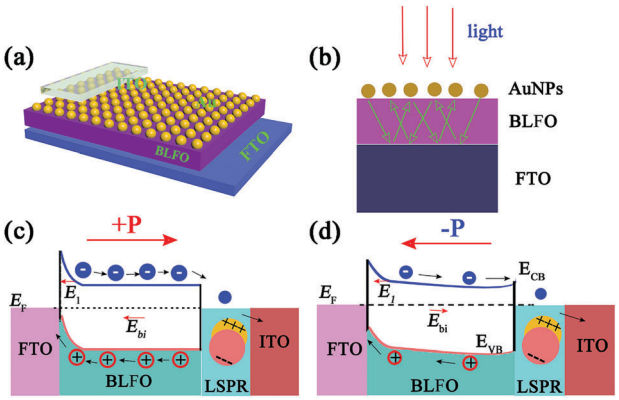

Fig. 7 (a) Schematic view of the PV device layout. (b) Schematic illustrating light trapping by the scattering from the metal nanoparticles. Energy band diagram of the ITO/AuNPs/BLFO/FTO device under the influence of AuNPs LSPR at positive (c) and negative (d) poling states.

both positive poling and AuNPs SP could enhance the PV output of the BLFO film. In addition, it seems that the tunability under the synergistic effect of AuNPs SP and positive poling is bigger than that under either AuNPs SP or positive poling. As indicated from the data in Table 2, the tunability for AB to I, A to I and B to I is not a simple superposition relationship, which gives clear evidence of the synergistic effect between the SP effect and ferroelectric polarization. A similar experimental phenomenon has been reported in terms of an increase in current density; however the physical mechanism still needs to be further elucidated.[15] The insets in Fig. 6a and b show the time-dependent photocurrent density under short-circuit conditions with the light being switched ON and OFF, which not only further confirms the modulation of PV output by the SP effect and ferroelectric polarization, but also exhibits an instantaneous and repeatable response of the photocurrent. It is obvious that the J_{SC} remains almost unchanged during 5 cycles of ON–OFF light illumination. Moreover, no spikes were found in the ON–OFF curves, which indicates that the Joule heating effect on the photocurrent is negligible.[52] The obvious ON/OFF photocurrent density ratio makes it possible for the BLFO film to be applied in the field of photosensitive resistors and memory devices.

Fig. 7a presents a schematic view of the Au NPs decorated ITO/BLFO/FTO device. To further clarify the operation mechanism of ITO/AuNPs/BLFO/FTO, the energy band diagrams of the PV device were schematically plotted in Fig. 7c and d. As has been noted, photo-generated electron–hole pairs can be separated under the combined effect of E_{bi} and E_1 when ITO /BLFO/FTO is illuminated. When the device of ITO/AuNPs/BLFO/FTO was illuminated, this photoelectric process can be strengthened once a set number of AuNPs with strong LSPR are modified on the BLFO surface. Under such a circumstance, in addition to the contribution from the BLFO/FTO potential barrier, the photocurrent increases, which is closely related to the SP mechanism. As shown in Fig. 7b, the AuNPs effectively scattered the incident light into the BLFO absorbing layer, thus increasing the optical path length in the thin film device.[53] Moreover, LSPR can intensify the optical field near the metal surfaces, and thus improve the absorption of incident photons. Generally, photo-induced carriers generated in the BLFO layer decay either radiatively or nonradiatively. Nevertheless, the AuNPs tightly attached to the BLFO layer favor the occurrence of charge transfer between long lifetime excitons and AuNPs, which confines the recombination of photo-generated pairs of electrons and holes.[54,55] Since the device is in a negative poling state (Fig. 7d), E_{bi} and E_1 have opposite directions, making it difficult to separate and transport electrons originating from the AuNPs SP effect and thus reduce the PV output. On the contrary, when the device is under a positive poling state (Fig. 7c), the direction of E_{bi} is the same as that of E_1. In this case, photo-generated carriers can easily migrate and transport, which favor the enhancement of the PV output. Furthermore, the intimate contact of the BLFO film with AuNPs enables the transfer of photo-generated electrons from BLFO to Au, thus reducing carrier recombination. Consequently, it is easy to understand that the ferroelectric polarization and the SP effect can affect and strengthen each other in the positive poling state. The modulation of SP excitation using polarization directions can offer an opportunity to optimize the effective optical absorption of BLFO films containing AuNPs.

Conclusion

In summary, La-doped BFO films were fabricated *via* a sol–gel method and spin-coating technology. The BLFO film with macroscopic ferroelectric property showed a polarization-tuned PV effect. Based on the UV-vis absorption spectra, it is obvious that the AuNPs exhibit an obvious LSPR effect for the device configuration of ITO/AuNPs/BLFO/FTO, which provides an efficient approach to increase the PV effect of BLFO films. Under the synergistic effect of AuNPs SP and positive poling, a significant increase in J_{SC} and V_{OC} from 5.3 μA cm^{-2} to 20 μA cm^{-2} and 0.2 V to 0.4 V was observed, which corresponded to the tunabilities of 100% and 277%, respectively. Considering the ferroelectric polarization and LSPR effect, a plausible theoretical model was schematically plotted to illustrate the physical mechanism of PV enhancement. This work provides a simple and robust method to develop inexpensive ferroelectric film based PV devices.

Conflicts of interest

There are no conflicts to declare.

Acknowledgements

The authors gratefully acknowledge the support from the National Natural Science Foundation of China (NSFC No. 51372069, 51472118, U1504624, 51671182), the Scientific and Technological Project in Henan Province (172102210013), and the Technology Innovation Talents in University of Henan Province (14HASTIT038). Prof. Zheng would like offer his special thanks to the scholarship under the International Cultivation of Henan Advanced Talents.

References

1 C.-H. Chiu, C.-W. Huang, Y.-H. Hsieh, J.-Y. Chen, C.-F. Chang, Y.-H. Chu and W.-W. Wu, *Nano Energy*, 2017, **34**, 103–110.
2 S. R. Basu, L. W. Martin, Y. H. Chu, M. Gajek, R. Ramesh, R. C. Rai, X. Xu and J. L. Musfeldt, *Appl. Phys. Lett.*, 2008, **92**, 091905.
3 W. Zhang, M.-M. Yang, X. Liang, H.-W. Zheng, Y. Wang, W.-X. Gao, G.-L. Yuan, W.-F. Zhang, X.-G. Li, H.-S. Luo and R.-K. Zheng, *Nano Energy*, 2015, **18**, 315–324.
4 C. Mix and G. Jakob, *J. Appl. Phys.*, 2013, **113**, 17D907.
5 H. Fan, Z. Fan, P.-L. Li, F.-Y. Zhang, G. Tian, J.-X. Yao, Z.-W. Li, X. Song, D.-Y. Chen, B. Han, M. Zeng, S.-J. Wu, Z. Zhang, M.-H. Qin, X.-B. Lu, J.-W. Gao, Z.-X. Lu, Z. Zhang, J.-Y. Dai, X.-S. Gao and J.-M. Liu, *J. Mater. Chem. C*, 2017, **5**, 3323–3329.
6 F. Wu, Y.-P. Guo, B. Guo, Y.-Y. Zhang, H. Li and H.-Z. Liu, *J. Phys. D: Appl. Phys.*, 2013, **46**, 365304.
7 V. S. Puli, D. K. Pradhan, R. K. Katiyar, I. Coondoo, N. Panwar, P. Misra, D. B. Chrisey, J. F. Scott and R. S. Katiyar, *J. Phys. D: Appl. Phys.*, 2014, **47**, 075502.
8 Y.-L. Liu, J. Wei, Y.-X. Guo, T.-T. Yang and Z. Xu, *RSC Adv.*, 2016, **6**, 96563–96572.
9 M. Kumar and K. Yadav, *Appl. Phys. Lett.*, 2007, **91**, 242901.
10 C.-C. Lee and J.-M. Wu, *Electrochem. Solid-State Lett.*, 2007, **10**, G58.
11 Y.-M. Sung, Y.-C. Lai, M.-F. Tsai, H.-H. Hsieh, M.-H. Yang, P. P. Wei, C.-S. Yeh, F.-C. Hsu and Y.-F. Chen, *J. Mater. Chem. C*, 2016, **4**, 513–520.
12 C.-Y. Wang, D.-W. Cao, F.-G. Zheng, W. Dong, L. Fang, X.-D. Su and M.-R. Shen, *Chem. Commun.*, 2013, **49**, 3769–3771.
13 J. Zuloaga and P. Nordlander, *Nano Lett.*, 2011, **11**, 1280–1283.
14 F. Lükermann, U. Heinzmann and H. Stiebig, *Appl. Phys. Lett.*, 2012, **100**, 253907.
15 Y. L. Huang, W. S. Chang, C. N. Van, H. J. Liu, K. A. Tsai, J. W. Chen, H. H. Kuo, W. Y. Tzeng, Y. C. Chen, C. L. Wu, C. W. Luo, Y. J. Hsu and Y. H. Chu, *Nanoscale*, 2016, **8**, 15795–15801.
16 F.-G. Zheng, P. Zhang, X.-F. Wang, W. Huang, J.-X. Zhang, M.-R. Shen, W. Dong, L. Fang, Y.-B. Bai, X.-Q. Shen, H. Sun and J.-H. Hao, *Nanoscale*, 2014, **6**, 2915–2921.
17 R. Maruyama, W. Sakamoto, I. Yuitoo, T. Takeuchi, K. Hayashi and T. Yogo, *Jpn. J. Appl. Phys.*, 2016, **55**, 10TA14.
18 J. Liu, M.-Y. Li, L. Pei, B.-F. Yu, D.-Y. Guo and X.-Z. Zhao, *J. Phys. D: Appl. Phys.*, 2009, **42**, 115409.
19 S. Singh, C. Tomy, T. Era, M. Itoh and H. Ishiwara, *J. Appl. Phys.*, 2012, **111**, 102801.
20 T. Zheng and J.-G. Wu, *J. Mater. Chem. C*, 2015, **3**, 11326–11334.
21 J.-Z. Huang, Y. Wang, Y.-H. Lin, M. Li and C. W. Nan, *J. Appl. Phys.*, 2009, **106**, 063911.
22 S.-T. Zhang, Y. Zhang, M.-H. Lu, C.-L. Du, Y.-F. Chen, Z.-G. Liu, Y.-Y. Zhu, N.-B. Ming and X. Q. Pan, *Appl. Phys. Lett.*, 2006, **88**, 162901.
23 K.-G. Yang, S.-H. Yang and Y.-L. Zhang, *Ferroelectrics*, 2010, **410**, 63–68.
24 A. Kumar, R. C. Rai, N. J. Podraza, S. Denev, M. Ramirez, Y.-H. Chu, L. W. Martin, J. Ihlefeld, T. Heeg and J. Schubert, *Appl. Phys. Lett.*, 2008, **92**, 121915.
25 J. Ihlefeld, N. Podraza, Z. Liu, R. Rai, X. Xu, T. Heeg, Y. Chen, J. Li, R. Collins and J. Musfeldt, *Appl. Phys. Lett.*, 2008, **92**, 142908.
26 P. S. V. Mocherla, C. Karthik, R. Ubic, M. S. Ramachandra Rao and C. Sudakar, *Appl. Phys. Lett.*, 2013, **103**, 022910.
27 N. Kumar, A. Kaushal, C. Bhardwaj and D. Kaur, *Optoelectron.: Adv. Mater. Devices*, 2010, **4**, 1497–1502.
28 G. Gopal Khan, R. Das, N. Mukherjee and K. Mandal, *Phys. Status Solidi RRL*, 2012, **6**, 312–314.
29 J.-B. Song, F. Wang, X.-Y. Yang, B. Ning, M. G. Harp, S. H. Culp, S. Hu, P. Huang, L.-M. Nie, J.-Y. Chen and X.-Y. Chen, *J. Am. Chem. Soc.*, 2016, **138**, 7005–7015.
30 C. Castillo, G. Buono-core, C. Manzur, N. Yutronic, R. Sierpe, G. Cabello and B. Chornik, *J. Chil. Chem. Soc.*, 2016, **61**, 2816–2820.
31 C. Clavero, *Nat. Photonics*, 2014, **8**, 95–103.
32 G. D. Spyropoulos, M. M. Stylianakis, E. Stratakis and E. Kymakis, *Appl. Phys. Lett.*, 2012, **100**, 213904.
33 S.-M. C. J.-K. Tsai., T.-H. Meen, Y.-C. Lin, T.-C. Wu, T.-Y. Chang, W. W. L.-W. Ji, W.-R. Chen, I.-T. Tang and C.-J. Huang, *Nanoscale Res. Lett.*, 2013, **8**, 450.
34 M. M. Giangregorio, M. Losurdo, G. V. Bianco, E. Dilonardo, P. Capezzuto and G. Bruno, *Mater. Sci. Eng., B*, 2013, **178**, 559–567.
35 S.-U. Park, R. Sharma, J.-K. Sim, B. J. Baek, H.-K. Ahn, J. S. Kim and C.-R. Lee, *Appl. Surf. Sci.*, 2013, **280**, 757–763.
36 D.-W. Cao, C.-Y. Wang, F.-G. Zheng, W. Dong, L. Fang and M.-R. Shen, *Nano Lett.*, 2012, **12**, 2803–2809.
37 R. Nechache, C. Harnagea, S. Li, L. Cardenas, W. Huang, J. Chakrabartty and F. Rosei, *Nat. Photonics*, 2014, **9**, 61–67.
38 R. Eskandari, X. Zhang and L. M. Malkinski, *Appl. Phys. Lett.*, 2017, **110**, 121105.
39 P. Yilmaz, D. Yeo, H. Chang, L. Loh and S. Dunn, *Nanotechnology*, 2016, **27**, 345402.
40 Y.-P. Guo, B. Guo, W. Dong, H. Li and H.-Z. Liu, *Nanotechnology*, 2013, **24**, 275201.
41 W. Dong, Y. P. Guo, B. Guo, H. Li, H. Z. Liu and T. W. Joel, *ACS Appl. Mater. Interfaces*, 2013, **5**, 6925–6929.

42 P. Maksymovych, S. Jesse, P. Yu, R. Ramesh, A. P. Baddorf and S. V. Kalinin, *Science*, 2009, **324**, 1421–1425.
43 W.-D. Wu, J. R. Guest, Y. Horibe, S. Park, T. Choi, S. W. Cheong and M. Bode, *Phys. Rev. Lett.*, 2010, **104**, 217601.
44 H.-W. Zheng, X.-Y. Liu, C.-L. Diao, Y.-Z. Gu and W.-F. Zhang, *Phys. Chem. Chem. Phys.*, 2012, **14**, 8376–8381.
45 I. Grinberg, D. V. West, M. Torres, G. Gou, D. M. Stein, L. Wu, G. Chen, E. M. Gallo, A. R. Akbashev, P. K. Davies, J. E. Spanier and A. M. Rappe, *Nature*, 2013, **503**, 509–512.
46 K. Sugawa, T. Tamura, H. Tahara, D. Yamaguchi, T. Akiyama, J. Otsuki, Y. Kusaka, N. Fukuda and H. Ushijima, *ACS Nano*, 2013, **7**, 9997–10010.
47 W.-G. Tu, Y. Zhou, H.-J. Li, P. Li and Z.-G. Zou, *Nanoscale*, 2015, **7**, 14232–14236.
48 S. Bai, J. Jiang, Q. Zhang and Y. Xiong, *Chem. Soc. Rev.*, 2015, **44**, 2893–2939.
49 S.-Y. Jin, E. DeMarco, M. J. Pellin, O. K. Farha, G. P. Wiederrecht and J. T. Hupp, *J. Phys. Chem. Lett.*, 2013, **4**, 3527–3533.
50 D. Szwarcman, D. Vestler and G. Markovich, *ACS Nano*, 2010, **5**, 507–515.
51 J.-Z. Xin, K.-C. Hui, K. Wang, H. L. W. Chan, D. H. C. Ong and C. W. Leung, *Appl. Phys. A: Mater. Sci. Process.*, 2012, **107**, 101–107.
52 R. K. Katiyar, Y. Sharma, P. Misra, V. S. Puli, S. Sahoo, A. Kumar, J. F. Scott, G. Morell, B. R. Weiner and R. S. Katiyar, *Appl. Phys. Lett.*, 2014, **105**, 172904.
53 X. Chen, B.-H. Jia, J. K. Saha, B. Cai, N. Stokes, Q. Qiao, Y.-Q. Wang, Z.-Y. Shi and M. Gu, *Nano Lett.*, 2012, **12**, 2187–2192.
54 S. Li, J.-M. Zhang, M. G. Kibria, Z. Mi, M. Chaker, D. Ma, R. Nechache and F. Rosei, *Chem. Commun.*, 2013, **49**, 5856–5858.
55 P. Biswas, S. R. Cho, J. W. Kim, S. D. Baek and J. M. Myoung, *Nanotechnology*, 2017, **28**, 225502.